

A high-temperature furnace for *in situ* synchrotron X-ray spectroscopy under controlled atmospheric conditions

Sigrid Griet Eeckhout,^{a*} Bernard Gorges,^a Laurent Barthe,^b Orietta Pelosi,^c Olga Safonova^a and Gabriele Giuli^c

^aEuropean Synchrotron Radiation Facility, BP 220, 38043 Grenoble, France, ^bSynchrotron Soleil, BP 48, 91192 Gif-sur-Yvette, France, and ^cUniversity of Camerino, Via Gentile III da Varano, 62032 Camerino, Italy. E-mail: eeckhout@esrf.fr

A high-temperature furnace with an induction heater coil has been designed and constructed for *in situ* X-ray spectroscopic experiments under controlled atmospheric conditions and temperatures up to 3275 K. The multi-purpose chamber design allows working in backscattering and normal fluorescence mode for synchrotron X-ray absorption and emission spectroscopy. The use of the furnace is demonstrated in a study of the *in situ* formation of Cr oxide between 1823 K and 2023 K at $\log PO_2$ values between -10.0 and -11.3 using X-ray absorption near-edge spectroscopy. The set-up is of particular interest for studying liquid metals, alloys and other electrically conductive materials under extreme conditions.

© 2008 International Union of Crystallography
Printed in Singapore – all rights reserved

Keywords: spectroscopy furnace; XANES; high temperature; extreme conditions.

1. Introduction

The local and electronic structure of materials and their changes during solid-state reactions and transformation processes can be investigated *in situ* by using X-ray absorption and emission spectroscopy (Glatzel & Bergmann, 2005). Since many interesting physical phenomena exhibited by materials occur at non-ambient temperatures, high-temperature devices have been constructed for many years (Berry *et al.*, 2003; Farges *et al.*, 1995, 1996, 1999; Filippini & Diccico, 1994; Filippini & Malvestuto, 2003; Jacobs & Egry, 1999; Marcos *et al.*, 1994; Munozpaez *et al.*, 1995; Safonova, Deniau *et al.*, 2006; Safonova *et al.*, 2005). The melting temperature of most metals is, however, very high, making it difficult to find a proper heater and a crucible material which resists such temperatures and does not react with the sample. Induction is a non-contact heating process which relies on induced electrical currents within the sample to produce heat. This process allows attaining temperatures up to 3275 K under different atmospheric conditions.

Our furnace combines the design by Jacobs & Egry (1999) to use induction heating in order to attain temperatures up to 3275 K and the design used in solid-state chemistry and catalysis to work under controlled atmospheric conditions (Grunwaldt *et al.*, 2001; Safonova *et al.*, 2005; Safonova, Tromp *et al.*, 2006). The furnace of Filippone and co-workers (Filippini & Diccico, 1994; Filippini & Malvestuto, 2003) also reaches such high temperatures but is operational under high-vacuum conditions. Furthermore, our furnace can be used for

X-ray absorption spectroscopy (XAS) measurements at lower energies, down to the Sc *K*-edge at 4492 eV. Compared with the design of Berry *et al.* (2003) for the study of Cr in silicate melts under controlled oxygen fugacities, the presented furnace reaches higher temperatures.

To demonstrate the operation of the apparatus we have chosen to study *in situ* the formation of chromium oxide on Cr metal under high temperature and low oxygen fugacity conditions for the following reasons.

(i) Chromium oxides exist in a range of oxidation states with known coordination environment; hence they are very useful to serve as reference materials for XAS. The oxidation state of the chromium oxides has been determined by wet chemical analysis on quenched materials and the phase diagram subsequently calculated (Toker *et al.*, 1991; Wilhelmi, 1968). However, owing to the fact that Cr^{2+} ions are rare and unstable in terrestrial minerals, *in situ* observation becomes almost unavoidable. $Cr^{2+}O$ is metastable at all temperatures and only exists in the liquid phase together with solid Cr_2O_3 (Degerov & Pelton, 1996). Furthermore, the oxidation state determined from quenched materials does not necessarily correspond to that present at high temperature because of the possibility of disproportionation or charge-transfer reactions on cooling (Berry & O'Neill, 2004; Berry *et al.*, 2003; Eeckhout *et al.*, 2007).

(ii) The study of the electronic structure and local coordination of Cr is important in geosciences and catalysis. Traditional trace-element studies have shown that minor amounts of Cr are present in the Earth's mantle (~ 0.3 wt% Cr_2O_3 is

believed to be present in the primitive mantle; O'Neill & Palmer, 1998). Changes in the oxidation state of transition elements, which have been predicted to be induced by high pressure (Li *et al.*, 1995), are critical for their partitioning behaviour during differentiation processes. Eeckhout *et al.* (2007) showed that in synthetic iron-free Cr:MgO the Cr²⁺ content reaches ~40%, and in Cr:MgSiO₃ perovskite with 0.006 Cr a.p.f.u. (atoms per formula unit) chromium is mainly divalent. Both phases are found in the Earth's lower mantle. In catalysis, supported chromium oxide is widely used in many industrial applications, the most important being the dehydrogenation of light alkanes over alumina-supported chromium oxides and the polymerization of ethylene over silica-supported chromium oxides (Weckhuysen *et al.*, 1996).

(iii) As the Cr *K*-edge lies below 6 keV, only few applications on Cr *K*-edge XAS have been reported in the literature (Berry & O'Neill, 2004; Berry *et al.*, 2003; Eeckhout *et al.*, 2007; Groppo, Lamberti *et al.*, 2005; Groppo, Prestipino *et al.*, 2005; Sutton *et al.*, 1993).

Highly pure chromium metal was used as a starting material and the different stability fields of the calculated phase diagram for chromium oxide were investigated by changing both temperature and atmospheric conditions. The fluorescence X-ray absorption near-edge spectra (XANES) measured *in situ* at the Cr *K*-edge are presented.

2. Technical characteristics

The experimental set-up of the high-temperature furnace is shown in Fig. 1. The chamber, 200 mm diameter and 275 mm height, is made from stainless steel. The inner side is shielded by highly pure Al foil to avoid any signal from the chromium present in the stainless steel. Secondary fluorescence radiation can be detected in backscattering mode by four photodiodes which are placed concentrically around the incident beam at 45° or with normal incident and grazing exit angle (detector at 90° with respect to the incoming X-ray beam). The photodiodes are connected to a voltage-to-frequency converter. The sensitivity of this converter is adjusted using an MCCE electrometer. The signal passes *via* fibre optics to the counting card. The furnace X-ray windows are made from 40 µm Kapton foil and have a diameter of 40 mm. The exit windows are additionally shielded by a black Kapton foil, hence resulting in a transmission of 85% at 6000 eV. Since the Kapton windows contain a small amount of Ca, the lower energy range is limited to the Sc *K*-edge at 4492 eV, where the transmission reaches 75%. Temperature is measured from the top by a multiwavelength pyrometer (FAR Associates SpectroPyrometer FMP2) with on-line tolerance and signal-strength (emissivity) display,

spectral and total emissivity correction and absorption compensation. For the non-contact temperature measurement a fused silica VP-DUV-200 viewport is used. An additional valve protects the viewport from metal sublimation in between two temperature measurements. The distance between sample and pyrometer was 23 cm. In order to check the temperature information derived from the pyrometer after calibration using an integrated laser, the melting temperature of Cr (99.7%+), Ni (99.9%) and Co (99.99%) metal was experimentally verified. For these measurements a piece of metal rod (2 mm diameter for Ni and Co and 5 mm diameter for Cr) was placed onto a BN holder and positioned within the induction coil. The chamber was first vacuum pumped and then filled with Ar inert gas, under a static pressure of 1 bar. The obtained temperature accuracy was 0.45%. The sample of 99.7%+ pure Cr metal (5 mm diameter) was then placed onto a BN holder and positioned within the induction coil. The height of the sample can be manually adjusted from the bottom of the chamber. The induction coil has an inner diameter of about 8 mm and a gap of about 1 mm between the two windings. This allows free observation of the sample from the side for the X-ray beam as well as for the detectors (Fig. 1). The basic components of the induction heating system are an AC power supply, induction coil and sample. The power supply sends alternating current through the coil, generating a magnetic field. When the sample is placed inside the coil, the magnetic field induces eddy currents in the sample, generating precise amounts of clean localized heat without any physical contact between the coil and the sample. The frequency of the alternating current within the Cu coil was about 300 kHz, hence the induction coil is water-cooled to avoid elevated temperatures and thus melting of the coil. The oxygen pressure *PO*₂ or redox potential inside the furnace was imposed by CO/CO₂ gas mixtures using computer-driven Bronkhorst mass-flow controllers. According to the reaction CO₂ → CO + 1/2 O₂, the ratio of CO and CO₂ accurately defines the partial

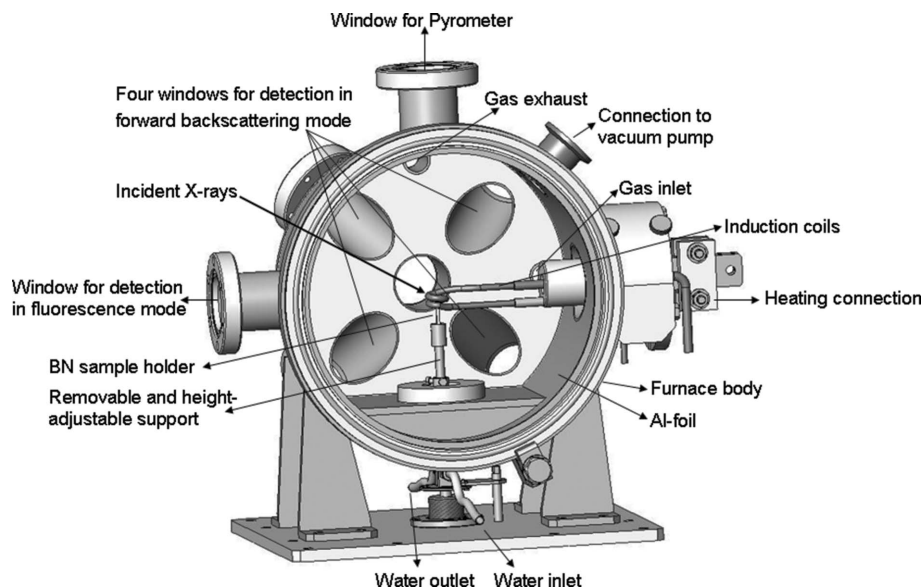


Figure 1 Experimental set-up of the high-temperature furnace.

pressure of oxygen. The used flow rates of CO and 1% CO₂ in He were between 27 and 100 ml min⁻¹. Before the experiment the chamber was evacuated to a pressure of $\sim 10^{-5}$ mbar, flushed by He and consequently filled and flushed twice by the desired gas mixture. The evacuation and filling procedure prevents the sample from being contaminated by atmospheric oxygen during subsequent heating. The chamber was maintained slightly above atmospheric pressure and the gases were vented to an extraction line.

Fluorescence-yield XANES were collected at the European Synchrotron Radiation Facility (ESRF) in Grenoble, France, at beamline ID26 (Gauthier *et al.*, 1999; Solé *et al.*, 1999). The storage ring operating conditions were 6 GeV electron energy and 200 mA electron current (hybrid mode). The energy of the incident synchrotron radiation beam was selected by means of a pair of He-cooled Si crystals (130 K) with a (220) orientation, providing an energy resolution of 0.35 eV at 6000 eV. A reference Cr metallic foil was used to provide an internal energy calibration for the monochromator (first inflection point of the Cr *K*-edge set at 5989 eV) at the beginning of each change of gas mixtures. We used two Si mirrors for the higher harmonics rejection of the incident X-ray beam (cut-off energy at 10 keV). XANES data were recorded in quick-scan mode by simultaneously scanning the monochromator angle and the undulator gap and counting 100 ms per point (Solé *et al.*, 1999). This continuous mode where the spectrum is collected ‘on the fly’ has further been reported by Frahm and co-workers (Bornebusch *et al.*, 1999; Frahm, 1989*a,b*; Lützenkirchen-Hecht & Frahm, 1999, 2001). The incident flux was monitored by detecting the X-ray scattering from a thin Kapton foil in the incident beam path. Fluorescence spectra were collected simultaneously in backscattering mode, *i.e.* with the scattering angle close to 180°, as well as with normal incident and grazing exit angle (Fig. 1). However, self-absorption effects cause considerable distortion of spectra measured in fluorescence mode (Pfalzer *et al.*, 1999; Troger *et al.*, 1992). These effects can be eliminated when measurements are taken at normal incidence and grazing exit angle (Pfalzer *et al.*, 1999), hence only the as-such obtained spectra will be discussed in this study. For XAS experiments on levitated metallic melts the backscattering mode is ideally suited (Jacobs & Egry, 1999). In addition, the spectrum measured within the stability field of Cr₂O₃ was compared with that of a Cr₂O₃ reference powder. The latter spectrum was recorded using a liquid-nitrogen-cooled Si (311) double-crystal monochromator, providing an energy resolution of 0.17 eV at 6000 eV. Each XANES within the energy range 5986–6004 eV took 30 s. The storage ring operating conditions were 6 GeV electron energy and 200 mA electron current ($2 \times 1/3$ filling mode). The other experimental conditions are the same as those for the furnace experiment.

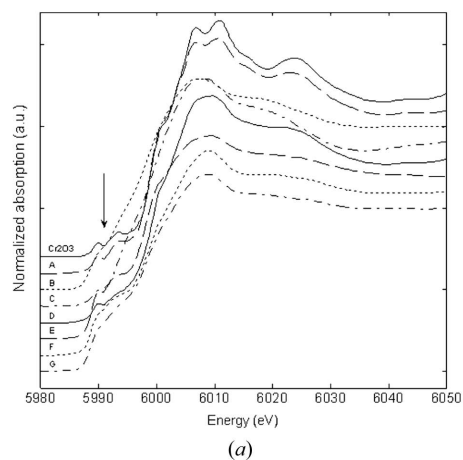
Table 1Pre-edge peak features of the Fe *K*-edge XANES spectra.Precision and accuracy of the pre-edge peak centroid are ~ 0.05 and 0.1 eV, respectively.

	Peak 1 (eV)	Peak 2 (eV)	Peak 1 FWHM (eV)	Peak 2 FWHM (eV)	Integrated intensity (arbitrary units)	Pre-edge centroid (eV)	Fit agreement index (%)
Cr ₂ O ₃	5989.9	5993.0	1.4	2.5	0.221	5991.9	99.9
<i>A</i>	5989.8	5993.0	1.4	2.4	0.267	5992.0	99.9
<i>B</i>	5989.9		2.8		0.112	5989.9	99.9
<i>C</i>	5989.5		1.8		0.070	5989.5	99.8
<i>D</i>	5989.9	5992.5	1.7	2.2	0.204	5990.9	99.9
<i>E</i>	5989.8	5992.5	2.2	2.8	0.938	5991.2	99.8
<i>F</i>	5989.8	5992.5	2.4	3.7	0.837	5991.5	99.9
<i>G</i>	5989.7	5992.4	2.2	4.2	0.755	5991.6	99.9

The XANES spectra were collected *in situ* between 2023 and 1823 K at different log *PO*₂ values in order to investigate the different chromium oxides (Toker *et al.*, 1991). At 2023 K the log *PO*₂ range was from -11.0 to -10.1 , at 1948 K from -11.3 to -11.0 , at 1923 K from -11.27 to -10.0 , and at 1823 K the log *PO*₂ value was -11.0 . The XANES spectra were normalized to the *K*-edge jump after subtraction of a constant background using the *WinXAS97* program (Ressler, 1997). Baseline subtraction was performed by fitting a Gaussian function on the low-energy tail of the edge starting at 5984 eV. The pre-edges were deconvoluted using the program *PeakFit4* into pseudo-Voigt components to derive the normalized height and position.

3. Applications

The use of XANES to determine the redox state and coordination number of transition metal cations generally relies on the analysis of the pre-edge features observed at the low-energy side of the edge. These features are related to dipole and quadrupole transitions from the metal *1s* core state to metal *3d* with some contribution from *4p* depending on the local symmetry. Their intensity and energy therefore depend on the valence state and site symmetry of the metal cation (Calas & Petiau, 1983; Farges, 2001; Giuli *et al.*, 2003; Sutton *et al.*, 1993; Westre *et al.*, 1997; Wilke *et al.*, 2001). The XANES reference spectrum for Cr³⁺ together with some selected spectra are depicted in Fig. 2. Four different groups can be discerned (Table 1). Firstly, the XANES spectrum of the Cr³⁺ reference Cr₂O₃ and spectrum *A* (collected at 1823 K and a log *PO*₂ value of -11) show two small pre-edge features around 5989.9 and 5993.0 eV and a strong shoulder at 6001.4 eV. The relative intensity is stronger for the pre-edge component occurring at the highest energy. Secondly, spectra *B* and *C* (collected at 1923 K and a log *PO*₂ value of -11.3 and at room temperature and a log *PO*₂ value of -11.3 ; the latter spectrum was collected after heating was switched off while keeping the same atmospheric conditions) show a single pre-edge peak and a broad shoulder around 5996 eV. The energy position of the Cr *K*-edge, corresponding to the minimum energy required to promote a *1s* electron to the continuum, is shifted by ~ 2.5 eV to lower energy with respect to that for the



Cr^{3+} reference. Thirdly, spectrum *D* (collected at 1948 K and a $\log PO_2$ value of -11.27) also reveals two small pre-edge features. The pre-edge peak at the lowest energy has the highest relative intensity. The Cr *K*-edge energy position occurs at an intermediate value compared with that for the other two groups. Fourthly, spectra *E*, *F* and *G* (collected at 2023 K and $\log PO_2$ values of -10.4 , -10.25 and -10.1) have a much higher integrated intensity for the pre-edge features, whereas the separation between the two pre-edge components is less obvious. The energy position of the centroid is close to that for Cr_2O_3 (Table 1). According to the phase diagram (Toker *et al.*, 1991), spectrum *B* (group 2) has been collected at the eutectic point, spectrum *D* (group 3) in the stability field for Cr_3O_4 , and spectra *E*, *F* and *G* (group 4) in the liquid phase. It is important to note at this point that when the sample is partly (*B*) or completely (*E*, *F*, *G*) liquid, the pre-edge features become broader and less defined, whereas the integrated intensity becomes higher. This also explains why spectrum *C* is better resolved with respect to spectrum *B* and has a lower pre-edge peak intensity. Interestingly, whereas the melting point of Cr_2O_3 lies at 2708 K, that for CrO_3 and CrO_2 occur at 470 K and 673 K, respectively. To the best of our knowledge, the melting points of Cr_3O_4 and CrO are not known, but, for comparison, the melting point of Cr^{2+} oxalate occurs at 573 K. Moreover, spectrum *C* can thus be regarded as a reference for Cr^{2+}O , although we should keep in mind that it is impossible to know whether all chromium occurs as Cr^{2+} .

The pre-edge data (integrated intensity *versus* centroid energy position) are plotted in Fig. 3. Previous studies at the Fe *K*-edge revealed that, when comparing data of unknown samples with those of model compounds with known Fe oxidation state and coordination number, the contribution of

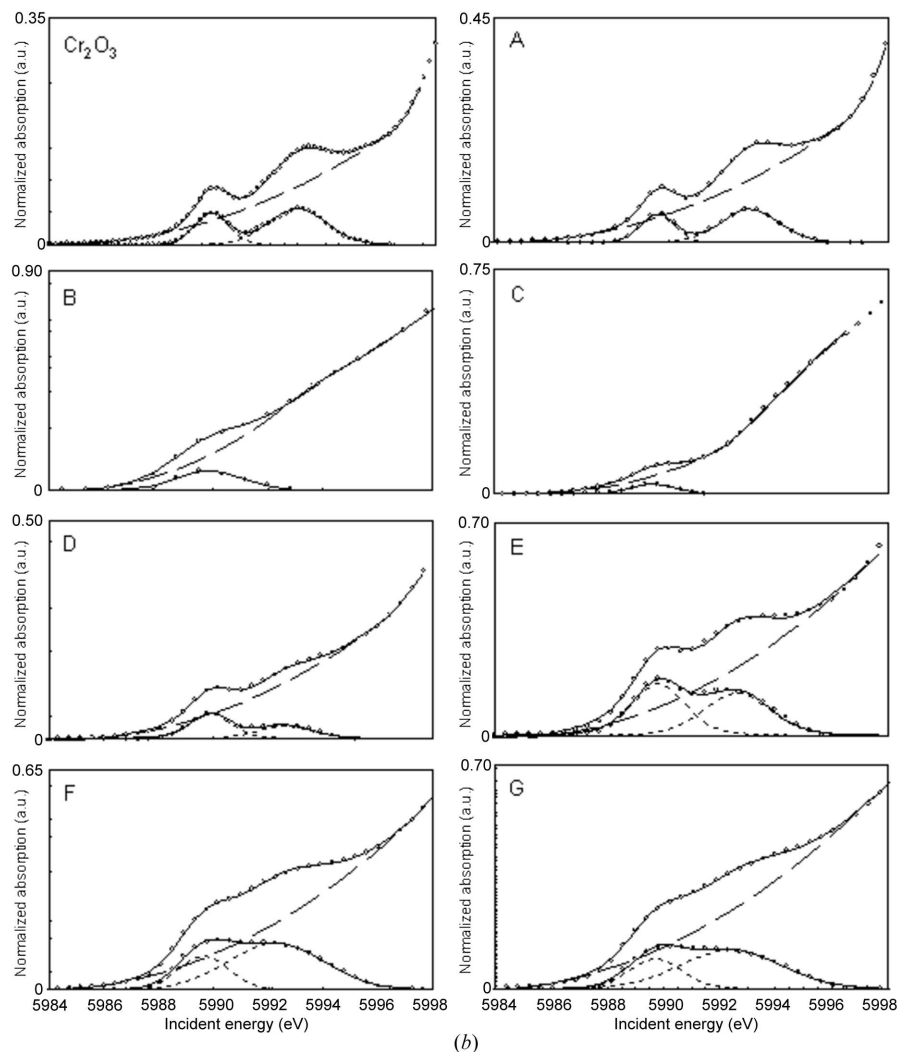


Figure 2

(a) XANES spectra of the Cr_2O_3 reference together with some selected spectra. The arrow points to the pre-edge features. Spectrum *A* was collected at 1823 K and a $\log PO_2$ value of -11 , *B* at 1923 K and -11.3 , *C* at room temperature and -11.3 , *D* at 1948 K and -11.27 , *E*, *F* and *G* at 2023 K and -10.4 , -10.25 and -10.1 , respectively. (b) Fit of the pre-edge features.

the different Fe oxidation states and coordination numbers can be evaluated (Farges, 2001; Giuli *et al.*, 2002, 2003, 2005; Wilke *et al.*, 2001). However, to the best of the author's knowledge, no XANES reference spectrum for Cr^{2+}O has been reported so far. So, in order to quantify the amount of Cr^{2+} in quenched silicate glass sample, Berry and co-workers (Berry & O'Neill, 2004; Berry *et al.*, 2003) used the shoulder at the edge crest. Groppo and co-workers (Groppo, Lamberti *et al.*, 2005; Groppo, Prestipino *et al.*, 2005) determined in a similar way *in situ* the Cr oxidation state of the Cr/SiO_2 catalyst. However, Glatzel *et al.* (2008) recently reported that in hematite ($\alpha\text{-Fe}_2\text{O}_3$) the pre-edge features reflect the strong influence of the orbital hybridization of metal–ligand and metal–metal type and are dominantly of dipolar character. Since the presently studied samples are partly or completely in the liquid phase, the shoulder at the edge crest is regarded not to be a suitable feature to determine the oxidation state. As a

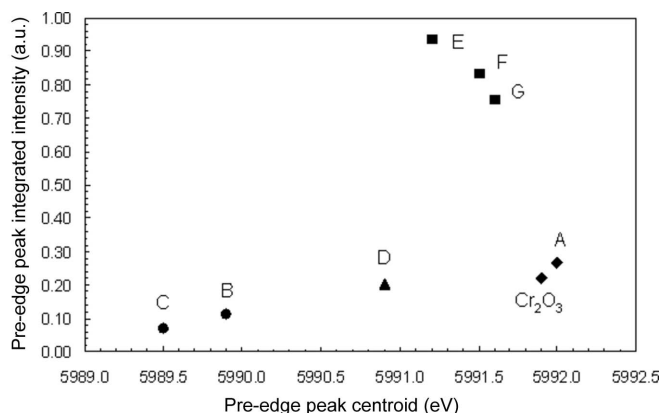


Figure 3 Plot of the pre-edge peak integrated intensity versus the centroid energy for the different samples belonging to group 1 (diamonds), group 2 (circles), group 3 (triangle) and group 4 (squares).

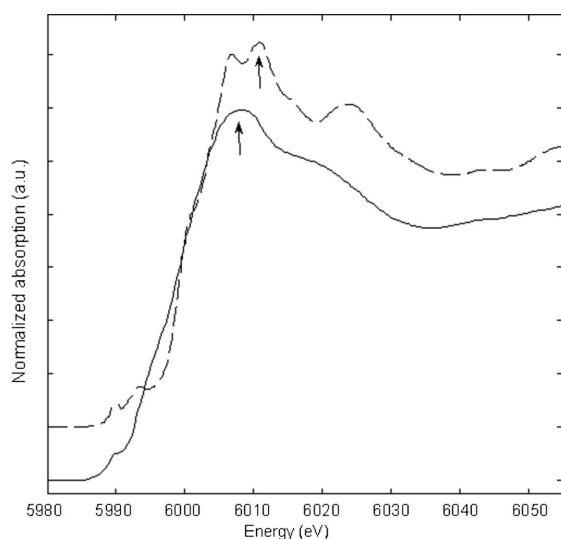


Figure 4 XANES spectra of the Cr²⁺O and Cr₂O₃ reference. The arrows point to the edge crest.

consequence, we use the centroid position of the pre-edge features to determine the Cr oxidation state, while the integrated intensity cannot be used to resolve the coordination number, as in the case of solid samples.

The centroid position for Cr³⁺ in Cr₂O₃ occurs at 5991.9 eV, whereas that for sample C, which is considered to be a reference for Cr²⁺O, occurs at 5989.5 eV. Fig. 3 reveals that group 1 represents the Cr³⁺ samples, group 2 the Cr²⁺ samples and group 3 the Cr²⁺–Cr³⁺ mixtures. The calculated liquid oxide phase (Toker *et al.*, 1991) at 2023 K and a log P_{O₂} value between –11.0 and –10.1 thus mainly consists of Cr³⁺, with small but varying amounts of Cr²⁺.

4. Concluding remarks

The use of our high-temperature furnace for *in situ* X-ray spectroscopic experiments under controlled atmosphere has been demonstrated in a study of the *in situ* formation of

chromium oxide. The calculated phase diagram for chromium oxide (Toker *et al.*, 1991) has been confirmed by experiment. At the calculated eutectic point (Toker *et al.*, 1991), chromium occurs mainly, if not completely, as Cr²⁺. When present in the liquid phase, the pre-edge features are more intense but less resolved. Chromium is then present as Cr³⁺, with small but varying amounts of Cr²⁺. Moreover, a reference spectrum for Cr²⁺O has been recorded (Fig. 4).

We acknowledge the ESRF for provision of synchrotron radiation facilities. Special thanks go to Yves Dabin, Heinz Graafisma, Peter Van der Linden, Thomas Neisius, Philippe Marion, Philippe Chappelet, Christophe Lapras and the ESRF staff. We are grateful for the critical comments expressed by two anonymous colleagues.

References

- Berry, A. J. & O'Neill, H. S. C. (2004). *Am. Mineral.* **89**, 790–798.
- Berry, A. J., Shelley, J. M. G., Foran, G. J., O'Neill, H. S. C. & Scott, D. R. (2003). *J. Synchrotron Rad.* **10**, 332–336.
- Bornebusch, H., Clausen, B. S., Steffensen, G., Lützenkirchen-Hecht, D. & Frahm, R. (1999). *J. Synchrotron Rad.* **6**, 209–211.
- Calas, G. & Petiau, J. (1983). *Solid State Commun.* **48**, 625–629.
- Degterov, S. & Pelton, A. D. (1996). *J. Phase Equilib.* **17**, 476–487.
- Eeckhout, S. G., Bolfan-Casanova, N., McCammon, C., Klemme, S. & Amiguet, E. (2007). *Am. Mineral.* **92**, 966–972.
- Farges, F. (2001). *Phys. Chem. Miner.* **28**, 619–629.
- Farges, F., Brown, G. E., Navrotsky, A., Gan, H. & Rehr, J. R. (1996). *Geochim. Cosmochim. Acta*, **60**, 3055–3065.
- Farges, F., Flank, A.-M., Lagarde, P. & Ténégal, F. (1999). *J. Synchrotron Rad.* **6**, 193–194.
- Farges, F., Itie, J. P., Fiquet, G. & Andrault, D. (1995). *Nucl. Instrum. Methods Phys. Res. B*, **101**, 493–498.
- Filippini, A. & Diccio, A. (1994). *Nucl. Instrum. Methods Phys. Res. B*, **93**, 302–310.
- Filippini, A. & Malvestuto, M. (2003). *Meas. Sci. Technol.* **14**, 875–882.
- Frahm, R. (1989a). *Physica B*, **158**, 342–343.
- Frahm, R. (1989b). *Rev. Sci. Instrum.* **60**, 2515–2518.
- Gauthier, C., Solé, V. A., Signorato, R., Goulon, J. & Moguiline, E. (1999). *J. Synchrotron Rad.* **6**, 164–166.
- Giuli, G., Eeckhout, S. G., Paris, E., Koeberl, C. & Pratesi, G. (2005). *Meteorit. Planet. Sci.* **40**, 1575–1580.
- Giuli, G., Paris, E., Pratesi, G., Koeberl, C. & Cipriani, C. (2003). *Meteorit. Planet. Sci.* **38**, 1181–1186.
- Giuli, G., Pratesi, G., Cipriani, C. & Paris, E. (2002). *Geochim. Cosmochim. Acta*, **66**, 4347–4353.
- Glatzel, P. & Bergmann, U. (2005). *Coord. Chem. Rev.* **249**, 65–95.
- Glatzel, P., Mirone, A., Eeckhout, S. G., Sikora, M. & Giuli, G. (2008). *Phys. Rev. B*, **77**, 115133.
- Groppo, E., Lamberti, C., Bordiga, S., Spoto, G. & Zecchina, A. (2005). *Chem. Rev.* **105**, 115–183.
- Groppo, E., Prestipino, C., Cesano, F., Bonino, F., Bordiga, S., Lamberti, C., Thune, P. C., Niemantsverdriet, J. W. & Zecchina, A. (2005). *J. Catal.* **230**, 98–108.
- Grunwaldt, J. D., Lützenkirchen-Hecht, D., Richwin, M., Grundmann, S., Clausen, B. S. & Frahm, R. (2001). *J. Phys. Chem. B*, **105**, 5161–5168.
- Jacobs, G. & Egry, I. (1999). *Phys. Rev. B*, **59**, 3961–3968.
- Li, J. P., Oneil, H. S. & Seifert, F. (1995). *J. Petrol.* **36**, 107–132.
- Lützenkirchen-Hecht, D. & Frahm, R. (1999). *J. Synchrotron Rad.* **6**, 591–593.
- Lützenkirchen-Hecht, D. & Frahm, R. (2001). *J. Phys. Chem. B*, **105**, 9988–9993.

- Marcos, E. S., Gil, M., Martinez, J. M., Munozpaez, A. & Marcos, A. S. (1994). *Rev. Sci. Instrum.* **65**, 2153–2154.
- Munozpaez, A., Gil, M., Martinez, J. M. & Marcos, E. S. (1995). *Physica B*, **209**, 241–242.
- O'Neill, H. St. C. & Palmer, H. (1998). *The Earth's Mantle – Composition, Structure and Evolution*, edited by I. Jackson, pp. 3–126. Cambridge University Press
- Pfalzer, P., Urbach, J. P., Klemm, M., Horn, S., denBoer, M. L., Frenkel, A. I. & Kirkland, J. P. (1999). *Phys. Rev. B*, **60**, 9335–9339.
- Ressler, T. (1997). *J. Phys. IV*, **7**, C2.
- Safonova, O. V., Deniau, B. & Millet, J. M. M. (2006). *J. Phys. Chem. B*, **110**, 23962–23967.
- Safonova, O. V., Neisius, T., Ryzhikov, A., Chenevier, B., Gaskov, A. M. & Labeau, M. (2005). *Chem. Commun.* pp. 5202–5204.
- Safonova, O. V., Tromp, M., van Bokhoven, J. A., de Groot, F. M. F., Evans, J. & Glatzel, P. (2006). *J. Phys. Chem. B*, **110**, 16162–16164.
- Solé, V. A., Gauthier, C., Goulon, J. & Natali, F. (1999). *J. Synchrotron Rad.* **6**, 174–175.
- Sutton, S. R., Jones, K. W., Gordon, B., Rivers, M. L., Bajt, S. & Smith, J. V. (1993). *Geochim. Cosmochim. Acta*, **57**, 461–468.
- Toker, N. Y., Darken, L. S. & Muan, A. (1991). *Metall. Trans. B*, **22**, 225–232.
- Troger, L., Arvanitis, D., Baberschke, K., Michaelis, H., Grimm, U. & Zschech, E. (1992). *Phys. Rev. B*, **46**, 3283–3289.
- Weckhuysen, B. M., Wachs, I. E. & Schoonheydt, R. A. (1996). *Chem. Rev.* **96**, 3327–3349.
- Westre, T. E., Kennepohl, P., DeWitt, J. G., Hedman, B., Hodgson, K. O. & Solomon, E. I. (1997). *J. Am. Chem. Soc.* **119**, 6297–6314.
- Wilhelmi, K. A. (1968). *Acta Chem. Scand.* **22**, 2565.
- Wilke, M., Farges, F., Petit, P. E., Brown, G. E. & Martin, F. (2001). *Am. Mineral.* **86**, 714–730.